Dalton Transactions

An international journal of inorganic chemistry

Accepted Manuscript

ROYAL SOCIETY OF CHEMISTRY

rsc.li/dalton

View Article Online
DOI: 10.1039/D0DT01788D

Near-IR Light-induced Photorelease of nitric oxide (NO) on Ruthenium Nitrosyl Complexes: Formation, reactivity aspects, and biological effects

Bishnubasu Giri [a], Taruna Saini[b], Sadananda Kumbhakar [a], Kalai Selvan K[a], Arabinda Muley[a], Ashish Misra[b]* and Somnath Maji*[a]

[a]*Department of Chemistry, Indian Institute of Technology, Hyderabad, Kandi, Sangareddy 502285*
Telangana, India
E-mail: smaji@chy.iith.ac.in

[b]*Department of Biotechnology, Indian Institute of Technology, Hyderabad, Kandi, Sangareddy 502285*
Telangana, India

View Article Online
DOI: 10.1039/D0DT01788D

Abstract

Polypyridyl backboned nitrosyl complexes of ruthenium with molecular framework $[Ru^{II}(antpy)(bpy)NO^{+/\bullet}]^{n+}$ [**4**]$(PF_6)_3$ (n = 3), [**4**]$(PF_6)_2$ (n = 2) where antpy = 4'-(anthracene-9-yl)-2,2':6',2''-terpyridine and bpy = 2,2'-bipyridine were synthesized by stepwise synthetic route from chloro precursor, $[Ru^{II}(antpy)(bpy)(Cl)](PF_6)$ [**1**](PF_6), via $[Ru^{II}(antpy)(bpy)(CH_3CN)](PF_6)_2$ [**2**]$(PF_6)_2$ and $[Ru^{II}(antpy)(bpy)(NO_2)](PF_6)$ [**3**](PF_6). After column chromatographic purification all synthesized complexes have been fully characterized by different spectroscopic and analytical techniques such as mass spectroscopy, ^1H NMR, FT-IR and UV-vis spectrophotometry. The Ru–NO stretching frequency of [**4**]$(PF_6)_3$ is observed at 1941 cm^{-1} which suggests moderately strong Ru–NO bonding. The massive shift in ν_{NO} frequency has taken place $\Delta\nu$ = 329 cm^{-1} (solid) by reducing [**4**]$(PF_6)_3$ to [**4**]$(PF_6)_2$. For understanding the molecular integrity the structure of [**3**](PF_6) has been successfully determined by X-ray crystallography. The redox properties of [**4**]$(PF_6)_3$ have been thoroughly investigated along with the other precursor complexes. Rate constants of the first order photo-release of NO from [**4**]$(PF_6)_3$ and [**4**]$(PF_6)_2$ have been determined at 8.01 x 10^{-3} min^{-1} ($t_{1/2}$ ~ 86 min) and 3.27 x 10^{-2} min^{-1} ($t_{1/2}$ ~ 21 min) respectively when exposed with Xenon 200 W light. Additionally, the photo-cleavage of the Ru–NO has been taken place throughout for ~2 h when [**4**]$(PF_6)_3$ was irradiated with an IR light source (>700 nm) at room temperature. The first-order rate constant at 9.4 x 10^{-3} min^{-1} ($t_{1/2}$ ~ 73 min) shows the efficacy of the system and its capability to release NO in the photo-therapeutic window. The light triggered released NO has been trapped by reduced myoglobin, a biologically relevant target protein. The one-electron reduction of [**4**]$(PF_6)_3$ to [**4**]$(PF_6)_2$ has been systematically carried out by chemically (hydrazine hydrate), electrochemically and biologically. In biological reduction, it has been found that the reduction is much slower with double-stranded DNA, compared to a single-stranded oligonucleotide (CAAGGCCAACCGCGAGAAGATGAC). Moreover, [**4**]$(PF_6)_3$ exhibits significant photo toxicity upon irradiation with the visible light source in the VCaP prostate cancer cell line (IC_{50} ~ 8.97 μM).

View Article Online
DOI: 10.1039/D0DT01788D

Introduction

The redox non-innocent small molecule, nitric oxide (NO) is prominent as one of the important mediators in a variety of pathological and physiological pathways such as immune response, neurotransmission, regulation of blood pressure, and cellular apoptosis.[1–5] NO synthase (NOS), the heme-containing enzyme catalyse L-arginine to synthesize nitric oxide, which is responsible for physiological disorders if it is deficient in human cells.[6] The typical drawbacks of NO drugs (such as glyceryl trinitrate) are due to its inexorability of NO release from NO donors.[7] However, poor selectivity of chemotherapeutic drugs towards the affected cells in comparison to healthy cells, a major drawback of chemotherapy, has encouraged the scientific community to develop novel approaches for site-specific delivery. One such approach is metallodrug activation by using light to attain spatiotemporal control at tumor site for the optimal release of active species. Metal nitrosyls could be the potential metallodrugs in chemotherapy due to its controlled photolabile behaviour. Although current literature has proved the efficacy of ruthenium nitrosyls to photo release activity and reliability towards photochemotherapy (PCT) and also photodynamic therapy (PDT), still an essential architecture of ruthenium nitrosyl framework is sought to be developed for next-generation cancer treatment.[8–10] For the development of an advanced ruthenium-based nitrosyl metallodrug, as a PCT agent, it is important to understand the non-innocent ligand characteristic nature of NO, because of its three unique available redox states: NO^+, $NO^\bullet$ and NO^- which makes NO as an encouraging ligand over the years from coordination perspectives.[11–13] In metmyoglobin, NO binds to central metal Fe as $[Fe^{II}–NO^+]$ while in reduced vitamin B_{12} as $[Co^{III}–NO^-]$.[14,15] From the last few decades, most of the photorelease study of nitrosyl complexes have been revealed on iron (Fe) and ruthenium (Ru) nitrosyl complexes.[16–19] Though the Fe-nitrosyl complexes have shown faster release of NO even in low energy light, but still not optimal for PDT due to its instability in the aqueous medium.[19–21] Most of the Ru-nitrosyl complexes are quite stable in the aqueous medium in comparable with first-row transition metal nitrosyl complexes but releasing NO from metal center associated with high energy UV radiation is an unpleasant condition for cells and tissues.[12,22,23] Among the various metal complexes studied, ruthenium complexes have revealed remarkable antitumor activity as they possess several advantages over platinum drugs, particularly low toxicity, less drug resistance, potent efficacy, and also are expected to have the potentiality of metal-based clinical antitumor drugs for the new generation.[24–26]

View Article Online
DOI: 10.1039/D0DT01788D

Although the ligand antpy has been described in the 19th century for metallosupramolecular system[27] and photoinduced process,[28] it has been explored in the 20th century more as a ruthenium complex for DNA cleavage,[29] DNA-photodamage,[30] temperature-controlled switchings between single and dual emission,[31] anion sensing,[32] and also in the luminescence studies.[33] Apart from this, Cu(II) complexes have been reported as photo-nucleases,[34] fluorescence imaging probe for L-Cysteine and cytotoxicity for cancer cells.[35] Co(II) and Fe(II) complexes have shown promising photo-cytotoxicity[36,37] and Cd(II) complex has been used for imaging agents in living cells.[38] Moreover, antpy-Eu(III) complexes have been exposed as phosphorescence probe for singlet oxygen,[39] the sensor for indole-3-acetic acid, and luminescence probe for mitochondrial singlet oxygen,[40,41] while Zn(II) and Ir(III) complexes as DNA-blocker and CO_2 detector respectively.[42,43] The ligand is also discussed in photophysics for Pt(II) complex and as oxovanadium(IV) complex in DNA crosslinking.[44,45] Very recently Pt(II) complex of antpy has shown high cytotoxicity in A2780 ovarian cancer cell lines.[46] As anthracenyl moiety is a biologically important fluorophore, the complexes containing this moiety could be appropriate for cellular imaging via fluorescence microscopy and photo-activated chemotherapy.[45] Therefore, 4'-(anthracene-9-yl)-2,2':6',2''-terpyridine (antpy) could be very suitable for fluorescence sensor as it possesses terpyridine as coordinating unit and anthracene as fluorescence tag. The substituent anthracene moiety can act together as a photosensitizer and a DNA binder.[47] For DNA photocleavage studies the organic chromophores namely anthracene is normally used due to the proper energies of its triplet excited states. An efficient channel may be provided by the anthacene like aryl chromophores to generate singlet oxygen ($^1O_2$) via the excitation of ^{1}MLCT of complex moiety with the help of energy transfer from triplet excited state of anthracene, ^{3}MLCT acts as an energy reservoir allowing it to relax in a much longer time domain.[30] Stitching of 9-anthracenyl moiety to the terpyridine backbone resulted a decrease of HOMO-LUMO gap, represented by a significant redshift in their absorption and emission.[48] According to our best knowledge, antpy based nitrosyl complex is not known to date in the current literature. For the first time we have developed a ruthenium nitrosyl based metallodrug for prostate cancer, integrating antpy as tridentate and 2,2'-bipyridine as a bidentate ancillary ligand in the octahedral framework.

In this present work, we have demonstrated a superior design and synthesis of Ru(II)-nitrosyl complex, integrated with tridentate ligand, anthracene-substituted terpyridine, 4'- (anthracene-9-yl)-2,2':6',2''-terpyridine (antpy) and bidentate ligand 2,2'-bipyridine (bpy),

View Article Online
DOI: 10.1039/D0DT01788D

$[Ru^{II}(antpy)(bpy)(NO^{+})](PF_6)_3$ [**4**]$(PF_6)_3$, along with its precursor complexes $[Ru^{II}(antpy)(bpy)(Cl)](PF_6)$ [**1**](PF_6), $[Ru^{II}(antpy)(bpy)(CH_3CN)](PF_6)_2$ [**2**]$(PF_6)_2$ and $[Ru^{II}(antpy)(bpy)(NO_2)](PF_6)$ [**3**](PF_6). Furthermore, we have synthesized the reduced nitrosyl complex, $[Ru^{II}(antpy)(bpy)(NO^{\bullet})](PF_6)_2$ [**4**]$(PF_6)_2$ chemically by using hydrazine hydrate, electrochemically and biologically both using DNA and oligonucleotide, used for expressing β-actin in human cells. For all the complexes, the spectroscopic analysis and redox properties have been carefully addressed. The structural elucidation of [**3**](PF_6) has been determined. The photo release kinetics of both the complexes, [**4**]$(PF_6)_3$ and [**4**]$(PF_6)_2$ have been studied in detail. The photo-released NO has been trapped by reduced myoglobin, a biologically relevant target protein. Moreover, NO has emerged as a potent anti-oncogenic agent in a variety of cancers including breast, cervical, and colorectal cancers.[49] In this study, we analyze the potency of ruthenium nitrosyl complex, $[Ru^{II}(antpy)(bpy)(NO^{+})](PF_6)_3$ [**4**]$(PF_6)_3$, which releases NO upon irradiation with visible Xenon light (200 W) on prostate cancer cell line (VCaP). Our results reveal that this complex exhibits significant phototoxicity in prostate cancer cells upon visible light irradiation.

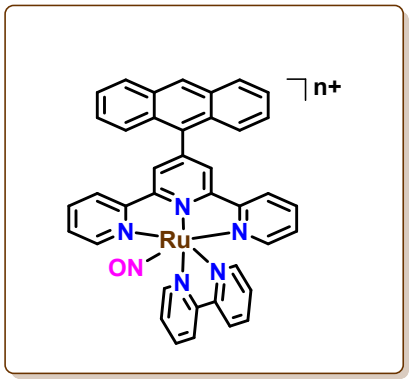

$\{NO^{+} \rightarrow (\mathbf{4}^{3+})\ NO^{\bullet} \rightarrow (\mathbf{4}^{2+})\}$

Results and discussion

Synthesis and Characterization

The tridentate meridional 4'-(anthracene-9-yl)-2,2':6',2''-terpyridine (antpy) ligand and the metal precursor $[Ru^{III}(antpy)Cl_3]$ are synthesized according to previously reported procedures.[28,50] Stepwise synthetic route has been adopted for the synthesis of $[Ru^{II}(antpy)(bpy)NO^{+}](PF_6)_3$ [**4**]$(PF_6)_3$, from $[Ru^{II}(antpy)(bpy)Cl](PF_6)$ [**1**](PF_6), chloro precursor via solvate acetonitrile,

View Article Online
DOI: 10.1039/D0DT01788D

$[Ru^{II}(antpy)(bpy)(CH_3CN)](PF_6)_2$ [**2**]$(PF_6)_2$ and nitro derivative, $[Ru^{II}(antpy)(bpy)(NO_2](PF_6)$ [**3**](PF_6) (Scheme 1) as all efforts have been failed for direct synthesis of pure [**4**]$(PF_6)_3$ from [**1**](PF_6), or [**2**]$(PF_6)_2$ using either NO gas or $NOBF_4$ which might be ascribed to the coordination saturation. The precursor chloro complex $[Ru^{II}(antpy)(bpy)Cl](PF_6)$ [**1**](PF_6) has been synthesized by refluxing ethanolic solution of ruthenium precursor $[Ru^{III}(antpy)Cl_3]$ and 2,2'-bipyridine (bpy) in presence of reducing agent triethylamine (Et_3N) and common ion salt LiCl. The solvate species [**2**]$(PF_6)_2$ has been synthesized on heating overnight with equimolar mixture of CH_3CN/H_2O and nitro precursor [**3**](PF_6) is prepared from complex [**2**]$(PF_6)_2$ on heating with excess aqueous $NaNO_2$ solution. Nitrosyl complex [**4**]$(PF_6)_3$ has been prepared from [**3**](PF_6) by using conc. HNO_3 and conc. $HClO_4$ at 0 °C, while the one-electron reduced radical complex, $[Ru^{II}(antpy)(bpy)(NO^{\bullet})](PF_6)_2$ [**4**]$(PF_6)_2$ has been formed by the reduction of [**4**]$(PF_6)_3$ chemically with hydrazine hydrate (Experimental section).

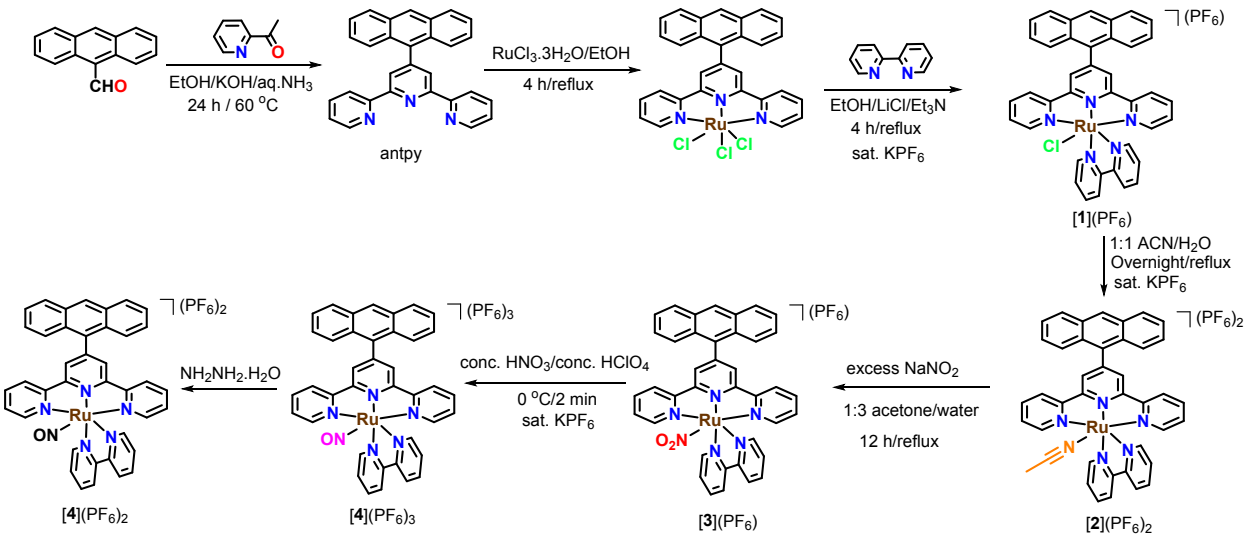

Scheme 1. Synthesis of [1](PF_6), [2]$(PF_6)_2$, [3](PF_6), [4]$(PF_6)_3$ and [4]$(PF_6)_2$

Though it is known that free NO_2^- undergoes disproportionation reaction to form NO_3^- and NO in presence of acid, metal bound nitrite does not disproportionate, it forms nitrosyl exclusively in presence of strong acid following the two step mechanism as shown below (Scheme 2).[51] The reason behind using of conc. HNO_3 and conc. $HClO_4$ is to avoid any unwanted side reactions.

View Article Online
DOI: 10.1039/D0DT01788D

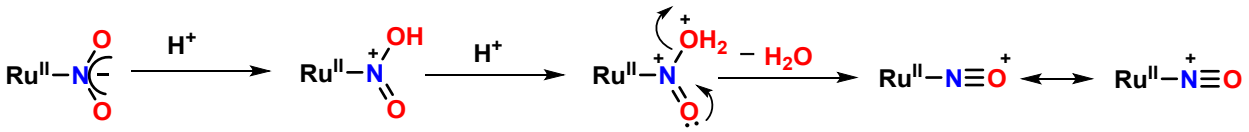

Scheme 2. Proposed mechanism for the conversion of complex [**3**](PF_6) into complex [**4**](PF_6)$_3$

In general, isolation of all complexes has been achieved via counter ion exchange with hexafluorophosphate salts and purified by column chromatography with neutral alumina. Satisfactory ^{1}H NMR data, FT-IR data, mass spectra, and electrical conductance authenticated their formation. Despite numerous efforts, we are unable to grow a suitable crystal of [**4**](PF_6)$_3$, but the single-crystal structure of [**3**](PF_6) has been successfully determined for understanding the molecular integrity (Fig. 1).

Crystallographic description

The nitro complex [**3**](PF_6) is crystallized by slow evaporation of 1:2 toluene and acetone solvent mixture and it exhibits distorted octahedral geometry in monoclinic crystal system with space group $P2_1/c$. Crystallographic data and important bond angles (°)/bond distances (Å) are shown in Table 1 and Table 2 respectively. The meridional site around ruthenium center is occupied by tridentate ligand, antpy and remaining three positions of the octahedral geometry are occupied by a bidentate ligand 2,2'-bipyridine (bpy) and the nitrogen atom of an anionic monodentate nitro group (Fig. 1), as reported earlier.[52,53] However, intra-ligand trans angle N1–Ru1–N3 of 158.3(1)° and other trans inter-ligand angles N2–Ru1–N5, N2–Ru1–N4 and N5–Ru1–N6 of 98.7(1)°, 175.4(1)° and 173.0(2)° respectively satisfy the condition of distorted octahedral geometry. Ru1–N2 bond length 1.969(3) Å is quite shorter than the corresponding Ru1–N1 and Ru1– N3 bond lengths 2.068(4) Å and 2.086(4) Å respectively, which is in harmony with previous reports.[52,54] The bond length of Ru1–N6 (2.027(4) Å) is as good as with previously reported structurally characterized similar complexes.[52,54,55] Moreover, anthracenyl and terpyridine moiety are almost in orthogonal position; torsional angle (C7–C8–C26–C39) is 88.2(8)°, whereas the torsional angle (N3–Ru1–N4–C16) between terpyridine moiety and bipyridine ligand is 98.3(4)°.

Spectral aspects

The ^{1}H NMR of diamagnetic complexes [**1**](PF_6), [**2**](PF_6)$_2$, [**3**](PF_6) and [**4**](PF_6)$_3$ reveal several overlaps of expected 27 protons in the aromatic region, of which nineteen protons are due to the meridional antpy ligand and other eight are due to the 2,2'-bipyridine ligand, (Table S1, Fig. S1–S4). Well-characterized deshielded doublets at 10.17, 9.74, 9.83 and 9.84 ppm are due to 2,2'-

View Article Online
DOI: 10.1039/D0DT01788D

bipyridyl ortho protons, which are adjacent to axial ligands X (X= Cl, CH_3CN, NO_2 and NO) in the complexes: [**1**](PF_6), [**2**](PF_6)$_2$, [**3**](PF_6) and [**4**](PF_6)$_3$ respectively, (Fig. S1–S4). Reason behind this noticeable downfield shift is formation of hydrogen bonding.[56] The characteristic terpyridyl singlet for two protons at 9.05, 9.18, 9.07 and 9.15 ppm and one signature singlet of anthracenyl proton at 8.92, 8.95, 8.94 and 8.76 ppm for [**1**](PF_6), [**2**](PF_6)$_2$, [**3**](PF_6) and [**4**](PF_6)$_3$ respectively, confirm the presence of antpy ligand backbone in all complexes.

MLCT (metal to ligand charge transfer) transitions, Ru(dπ) to π∗ orbitals of anthracene derived terpyridine ligand and 2,2'-bipyridine at 508 nm, 460 nm, 478 nm, 362 nm, and 485 nm are observed for the complexes [**1**](PF_6), [**2**](PF_6)$_2$, [**3**](PF_6)**,** [**4**](PF_6)$_3$ and [**4**](PF_6)$_2$ respectively (Fig. 2). Band energies (MLCT) follow the decreasing trend [**1**](PF_6) (508 nm) < [**4**](PF_6)$_2$ (485 nm) < [**3**](PF_6) (478 nm) < [**2**](PF_6)$_2$ (460 nm) < [**4**](PF_6)$_3$ (362 nm) in CH_3CN at room temperature, due to relative stability of dπ(Ru) energy levels. The noticeable blue shift of MLCT band for [**4**](PF_6)$_3$ indicates a strong back-bonding interaction of dπ(Ru^{II}) to π*(NO^+).[8,52,53,57]

The IR vibrational data for ν(PF_6^-) vibrations are summarized in Table S2 (Fig. S7–S11). The characteristic Ru–NO_2 frequencies for [**3**](PF_6) are observed at 1268 cm^{-1} (symmetric) and 1354 cm^{-1} (asymmetric) (Fig. S9). Stretching frequency of Ru–NO for [**4**](PF_6)$_3$ is observed at 1941 cm^{-1} which suggests moderately strong Ru–NO bonding. In previously reported terpyridine based ruthenium nitrosyl complexes, the Ru–NO stretching frequencies are relatively quite high with a combination of different strong π-acidic ligands (Table 4). In the present scenario, anthracene derivatized terpyridine has reduced NO stretching frequency significantly to 1941 cm^{-1}, suggesting the moderate electrophilic character of NO. Comparing related Ru–NO stretching frequencies with very similar molecular frameworks $[Ru^{II}(NNN)(NN)(NO^+)]^{3+}$, with meridional tridentate ligand (NNN = tpy)/strong π-acidic bidentate ligands (NN) where NN = pap, 1960 cm^{-1}; NN = bpm, 1957 cm^{-1}, NN = bpy, 1952 cm^{-1} and NN = pip, 1948 cm^{-1} are observed respectively. Also for facial tridentate ligand (NNN = {[9]aneS3}) and bidentate (NN) where NN = pap, 1964 cm^{-1}; NN = bpy, 1945 cm^{-1} and (NNN = tpm) with bidentate (NN) where NN = pap, 1962 cm^{-1}; NN = bpy, 1959 cm^{-1} are observed respectively. It is also worth mentioning that, with the strong σ-donor $acac^-$ ligand, Ru–NO stretching frequency is observed at 1914 cm^{-1} (Table 4 and ligand drawing). Introducing anthracene moiety has a big impact on reducing the stretching frequency of the Ru–NO complexes and this has been proved very useful in tuning the photo physical properties.

View Article Online
DOI: 10.1039/D0DT01788D

Though the previous reports have shown that ancillary ligands play an essential role for the Ru–NO bond electrophilic character, the present report demonstrates a new finding where appropriate electronic properties of tridentate ligand can help in lowering the NO stretching frequency. Upon one-electron reduction of [**4**]$(PF_6)_3$, the stretching frequency has been decreased from 1941 cm^{-1} to 1612 cm^{-1} (Fig. 3). This 329 cm^{-1} shift of frequency is due to occupancy of electron to the $\pi*$ orbital of NO which leads to decrease of bond order. The massive shift in ν_{NO} frequency, $\Delta\nu$ = 329 (solid) cm^{-1} by reducing [**4**]$(PF_6)_3$ to [**4**]$(PF_6)_2$ is associated with geometry change from linear Ru^{II}–NO^+, to most possible bent Ru^{II}–$NO^{\bullet}$.[52,54,55,58]

Redox properties

Because of the different electronic nature of monodentate ligands, the oxidation potentials of Ru(II)/(III) couples in CH_3CN at E^{o}_{298K}/V are observed at 0.806 V, 1.327 V and 1.052 V *vs* SCE (standard calomel electrode) for [**1**](PF_6), [**2**]$(PF_6)_2$ and [**3**](PF_6) respectively (Fig. S6 and Table 5). The redox couple systematically varies following the order of $Cl^- < NO_2^- < CH_3CN$. Relatively larger value of Ru(II)/(III) couple in [**3**](PF_6) than [**1**](PF_6), is because of stronger ligand field of NO_2^- compare to Cl^-. Correspondingly, the additional stability of Ru(II) state in [**2**]$(PF_6)_2$ is due to combined effect of ligand field strength and electrostatic factor for overall charge of $[\mathbf{2}]^{2+}$ as compare to $[\mathbf{3}]^+$ and $[\mathbf{1}]^+$. Sequential two one-electron reductions of tridentate acceptor ligand antpy appear in the potential range –0.621 V to –1.670 V for all the complexes while free antpy ligand has been reduced irreversibly in the potential window between –1.211 V to –1.512 V. But, in the case of [**4**]$(PF_6)_3$, the first reduction is found reversible while second one is irreversible. Ru(II)/(III) redox couple is not observed within experimental solvent (CH_3CN) potential edge +2.0 V *vs* SCE, due to the higher stabilization of Ru(II) oxidation state by strong π acidic antpy ligand. The redox potentials, appeared at 0.464 V and –0.177 V, are due to NO centered reduction, firstly [Ru^{II}–NO^+] to [Ru^{II}–$NO^{\bullet}$] and then [Ru^{II}–$NO^{\bullet}$] to [Ru^{II}–NO^-] respectively for [**4**]$(PF_6)_3$. The large comproportionation constant, Kc ($10^{10.9}$) {$RTln K$c = $nF(\Delta E)$}; (ΔE = difference in potential between the NO centered reductions), facilitates the isolation of intermediate complex [**4**]$(PF_6)_2$. For analogous ruthenium complexes, the potential for [Ru^{II}–NO^+] to [Ru^{II}–$NO^{\bullet}$] follows a satisfactory linear trend with various ligand combinations (listed in Table 4) and corresponding ν(NO) values (Fig. 4).

View Article Online
DOI: 10.1039/D0DT01788D

Drawing of ligands

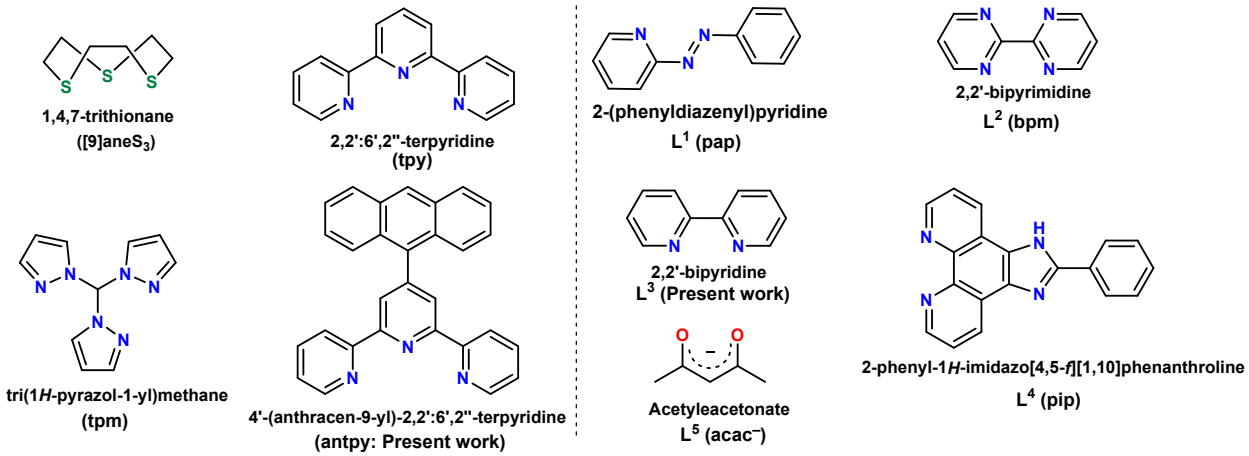

Light induced Ru–NO bond cleavage in $[4](PF_6)_3$ and $[4](PF_6)_2$

Both $[\mathbf{4}](PF_6)_3$ and $[\mathbf{4}](PF_6)_2$ are quite stable under normal ambient light condition in CH_3CN. Conversely, when visible Xenon light (200 W) source was exposed to degassed CH_3CN solution of both $[\mathbf{4}](PF_6)_3$ and $[\mathbf{4}](PF_6)_2$, the solutions were readily transformed to solvated species $[\mathbf{2}](PF_6)_2$ by a distinct colour change to orange, suggesting the Ru–NO bond cleavage. Formation of $[\mathbf{2}](PF_6)_2$ has been confirmed by distinct colour change and also by spectral change in UV-vis analysis. The photo-cleavage of $\{Ru^{II}–NO^+\}$ bond proceeds via the intermediate $\{Ru^{III}–NO^{\bullet}\}^*$ (S = 1 state) following equation (1)[8,22,59,60] and $\{Ru^{II}–CH_3CN\}$ species as confirmed by comparing with the spectra of synthesized solvated species $[\mathbf{2}](PF_6)_2$ after photo-cleavage.

$$\{Ru^{II}–NO^+\} + h\upsilon \rightarrow \{Ru^{III}–NO^{\bullet}\}^* \rightarrow \{Ru^{II}–CH_3CN\} + NO^{\bullet} \qquad (1)$$

Photo-cleavage of Ru–NO bond is executed throughout ~ 4 h for $[\mathbf{4}](PF_6)_3$, while for reduced radical species $[\mathbf{4}](PF_6)_2$, ~70 min, suggesting that photo-induced Ru(II)–NO bond cleavage is much faster for $[\mathbf{4}](PF_6)_2$ than $[\mathbf{4}](PF_6)_3$ under same photolytic conditions (Fig. 5a and 5b). The first-order rate constants for visible light-triggered NO release have been determined at 8.01 X 10^{-3} min^{-1}; half-life ($t_{1/2}$) = 86 min and 3.27 X 10^{-2} min^{-1}; half-life ($t_{1/2}$) = 21 min for $[\mathbf{4}](PF_6)_3$ and $[\mathbf{4}](PF_6)_2$ respectively. No change in the integrity of remaining molecular framework was observed which is very much significant from biological importance (Fig. 5c). However, $[Ru^{II}(tpy)(pip)(NO^+)]^{3+}$ complex does not undergo photo-cleavage of Ru–NO when it is exposed with 350 W visible xenon light, while the photo-cleavage of reduced $[Ru(tpy)(pip)(NO^{\bullet})]^{2+}$ has

View Article Online
DOI: 10.1039/D0DT01788D

been reported: (k_{NO}) = 2.0 X 10^{-1} min^{-1}; half-life ($t_{1/2}$) = 3.5 min.[52] Similarly, $[Ru(tpy)(pdt)(NO^{\bullet})]^{2+}$ (pdt: 5,6-diphenyl-3-pyridyl-as-triazine) complex has shown photorelease of NO with much slower rate (K_{NO}) = 4.4 X 10^{-3} min^{-1} ; half-life ($t_{1/2}$) = 157 min.[61] This indicates both [**4**]$(PF_6)_3$ and [**4**]$(PF_6)_2$ have superior potentiality towards light-triggered NO release under the mild condition via the attachment of 9-anthracenyl moiety to the terpyridine core.

Most significantly, when deoxygenated CH_3CN solution of [**4**]$(PF_6)_3$ was irradiated with an IR (>700 nm) light source (375 W) at room temperature, the photo-cleavage of the Ru–NO has been taken place throughout for ~2 h. The first-order rate constant is observed at 9.4 X 10^{-3} min^{-1}; half-life ($t_{1/2}$) = 73 min (Fig. 6). This study indicates the efficacy of the anthracene decorated terpyridine ruthenium nitrosyl complex and its capability to release NO in photo-therapeutic window, a suitable condition for better designing of PCT agents.

Photo-liberated NO trapping by Myoglobin (Mb)

After photolysis of [**4**]$(PF_6)_3$ and [**4**]$(PF_6)_2$, the liberated NO is passed through a deoxygenated aqueous solution of reduced myoglobin which has been prepared freshly with excess sodium dithionite to form an intense band at λ_{max} = 422 nm in electronic spectra following standard method.[62] This characteristic peak, due to Fe^{II}–NO bonding in myoglobin, confirms the formation of Mb–NO adduct. The myoglobin and reduced myoglobin showed intense peaks at 409 mm (Soret peak) and 433 nm respectively (Fig. 7)[12,57,63]

Biological reduction of [4]$(PF_6)_3$ to [4]$(PF_6)_2$

As DNA has single electron reducing ability due to the purine and pyrimidine bases, [**4**]$(PF_6)_3$ undergoes a slow one-electron reduction by an aqueous solution of salmon sperm DNA.[64,65] Deoxyguanosine monophosphate (dGMP), a monomer present in DNA, is mainly responsible for the reduction as the reduction potential of guanosine is lowest among all bases present in DNA.[66] The value of 1.02 V (NHE) oxidation potential measured for GMP in physiological buffer solution at pH 7.4. Also, [**4**]$(PF_6)_3$ was reduced to [**4**]$(PF_6)_2$ by an aqueous solution of oligonucleotide (CAAGGCCAACCGCGAGAAGATGAC); the oxidation potential for guanine 0.81 V (NHE) at pH 7.4.[67] The oligonucleotide is commonly used for understanding gene expression for human β-actin, a protein excessively available in cells and it activates the endothelial nitric oxide synthase (eNOS) enzyme to synthesis nitric oxide in the human body for different biological processes.[68] However, the reduction of [**4**]$(PF_6)_3$ to [**4**]$(PF_6)_2$ is much faster with oligonucleotide than with

View Article Online
DOI: 10.1039/D0DT01788D

DNA; most likely due to guanosine, which is easily exposed to nitrosyl complex, unlike the double-stranded DNA. (Fig. 8).

Live Cell Imaging

Photo-cytotoxic behaviour of [**1**](PF_6), [**2**]$(PF_6)_2$, [**3**](PF_6), [**4**]$(PF_6)_3$ and [**4**]$(PF_6)_2$ are studied in human prostate cancer cell line VCaP upon irradiation with the visible 200 W Xenon light (400-700 nm). VCap cells are incubated with these compounds for 6 h following which they are photo-irradiated using visible light. Substantial decrease in VCaP cell number is observed upon incubation with 3 μM of [**4**]$(PF_6)_3$ and [**4**]$(PF_6)_2$ for 6 h followed by photo-irradiation using visible light due to the facile labile nature of coordinated NO. No effect are observed in cells treated with [**1**](PF_6), [**2**]$(PF_6)_2$, [**3**](PF_6) because of the non-labile nature of the coordinated monodentate ligands (Cl^-, CH_3CN and NO_2^-) respectively. Also, no toxicity is observed in cells that are not irradiated with visible light upon incubation with the compounds (Fig. 9 and Fig. S12). These observations suggest that the treatment of the VCaP prostate cancer cells with [**4**]$(PF_6)_3$ and [**4**]$(PF_6)_2$ at the 3 μM and above concentrations are toxic to cells only upon visible light irradiation, while the complexes remain non-toxic to cells in dark.

Photo-cytotoxicity in VCaP cells

To understand the effect of visible light irradiation on the phototoxic effect of [**4**]$(PF_6)_3$ in VCaP cells, varying concentrations of the compound are used (Fig. 9). Cell viability is estimated for [**4**]$(PF_6)_3$ by 3-(4,5-dimethylthiazol-2-yl)-2,5-dimethyltetrazolium bromide (MTT) assay which involves the reduction of yellow MTT to insoluble coloured formazan crystals. Only viable cells are capable of carrying out this conversion and the quantity of formazan crystals reflects the number of live cells. We have examined the effect of [**4**]$(PF_6)_3$ on viability by treating the VCaP cells with varying concentrations of the complex. The control experiment did not exhibit any change in cell viability upon exposure to visible light, while the cells treated with [**4**]$(PF_6)_3$, exhibit significant photo-cytotoxicity with an IC_{50} value of ~8.97 μM upon irradiation with visible light (Fig. 10). Thus, our results suggest that [**4**]$(PF_6)_3$ exhibits cytotoxic behavior upon photo-activation with visible light irradiation.

Conclusion

The present work demonstrates design and synthesis of mononuclear ruthenium-based nitrosyl complexes [**4**]$(PF_6)_3$ and [**4**]$(PF_6)_2$, with molecular framework $[Ru^{II}(antpy)(bpy)(NO)]^{n+}$ {n = 3, [**4**]$(PF_6)_3$; n = 2, [**4**]$(PF_6)_2$}, in which the tridentate meridional ligand 4'-(anthracene-9-yl)-

View Article Online
DOI: 10.1039/D0DT01788D

2,2':6',2"-terpyridine (antpy) has shown significant impact on reducing the Ru–NO stretching frequency. X-ray single crystal structure of nitro precursor, [**3**](PF_6) has been determined to understand the integrity of the complexes. Along with all precursor complexes, the redox properties of [**4**]$(PF_6)_3$ have been thoroughly studied. The potentiality of photo-cleavage under visible Xenon light (200 W) as well as near IR light (375 W) irradiation with rate constants (K_{NO}) 8.01 X 10^{-3} min^{-1}; half-life ($t_{1/2}$) = 86 min and 9.4 x 10^{-3} min^{-1}; half-life ($t_{1/2}$) = 73 min respectively suggested [**4**]$(PF_6)_3$ is a suitable metallodrug for photochemotherapy (PCT) and the photo-triggered released NO has been trapped by reduced myoglobin (Mb). The one-electron reduction of [**4**]$(PF_6)_3$ to [**4**]$(PF_6)_2$ has been systematically carried out by chemically (hydrazine hydrate), electrochemically, and biologically. In biological reduction, it is found that the reduction is much slower with double-stranded DNA, compare to a single-stranded oligonucleotide (CAAGGCCAACCGCGAGAAGATGAC). Also, live-cell imaging and MTT assays have shown [**4**]$(PF_6)_3$ has remarkable photo-cytotoxic activity in VCaP cells (IC_{50} ~ 8.97 μM) upon irradiation with visible light. Overall, our study provides new leads to the development of photochemotherapeutic agents to combat prostate cancer.

Experimental

Materials

The precursor complex [Ru(antpy)Cl_3][50] and the ligand antpy were synthesized followed by the reported literature.[28] All chemicals and solvents were purchased from Sigma Aldrich, and used as received. HPLC grade and dry CH_3CN were used for spectroscopic and electrochemical studies respectively. The 375W E27 ES 230-250V IR blub was purchased from Amazon. Prostate cancer cell line VCaP was obtained from American Type Culture Collection (ATCC®).

Physical Measurements

^1H NMR spectral studies were performed in $(CD_3)_2SO$ at 298 K on Bruker Advance III-400 MHz spectrometer following the standard methods. Electron spray ionization (ESI) mass spectra were measured on Q-TOF mass spectrometer in CH_3CN. Electronic spectra were recorded on Jasco V-730 spectrophotometer in CH_3CN at 298 K. Cyclic voltammetric measurements (CV) were carried out on CHI-660 potentiostat. Electrochemical experiments were performed with a working electrode (3 mm glassy carbon); counter electrode (platinum wire), and a reference electrode (saturated calomel electrode (SCE)) under argon atmosphere in the standard three-electrode configuration with scan rate at 50 mV/s or 100 mV/s. Supporting electrolyte, TBAP (tetra butyl

View Article Online
DOI: 10.1039/D0DT01788D

ammonium perchlorate), was used after dissolving the complexes in CH_3CN and the concentration of the solution was ~10^{-3} M. The electrical conductivity of all the complexes were measured on Systronic Conductivity bridge 306. FT-IR spectra were recorded on Fourier transform Bruker Alpha-P spectrometer. Single X-ray crystal structure was measured on Oxford Xcalibur 2 diffractometer. Prostate cancer cell line (VCaP) was cultured in Thermo Fisher Scientific Direct Heat CO_2 incubator and live-cell imaging was performed using Nikon Inverted Research Microscope (ECLIPSE TS2R-FL).

Synthesis

Synthesis of $[Ru^{II}(antpy)(bpy)(Cl)]PF_6$ [1](PF_6)

$[Ru^{III}(antpy)Cl_3]$ (150 mg, 0.243 mmol), 2,2'-bipyridine (38 mg, 0.243 mmol), NEt_3 (0.6 mL) and excess LiCl (100 mg, 2.38 mmol) were placed in a double neck round bottom flask. 25 mL of EtOH was added and refluxed under argon saturated atmosphere for 4 h. Initial greenish solution slowly changed to a deep purple. The solvent was removed by using rotary evaporator to form a dry mass which was dissolved with minimal CH_3CN. Few drops of saturated aqueous KPF_6 was added to form a dark precipitate. Solid precipitate was washed with cold water after filtration and dried in desiccator. Crude product was further purified by column chromatography by using neutral alumina column, eluted with 5 % CH_3CN/CH_2Cl_2. Pure [**1**](PF_6) was afforded after evaporation of the solvent. Yield: 110 mg (64.46%). MS (ESI^+, CH_3CN), *m/z* Calcd for $[M–PF_6]^+$: 702.099; Found 702.11. Molar conductivity [$\Lambda_M(\Omega^{-1}\,cm^2\,M^{-1})$] in CH_3CN at 298 K: 112. ^1H NMR (400 MHz, $(CD_3)_2SO$, Me_4Si): δ_H (ppm): 10.17 (d, J = 4.96 Hz, 1 H), 9.04 (s, 2 H), 8.96 (d, J = 8.16 Hz, 1 H), 8.92 (s, 1 H), 8.74 (d, J = 8.12 Hz, 2 H), 8.70 (d, J = 8.08 Hz, 1 H), 8.40 (t, J = 7.84, 7.8 Hz, 1 H), 8.30 (m, 3 H), 8.09 (t, J = 6.92, 6.16 Hz, 1 H), 7.94 (t, J = 7.84, 7.76 Hz, 2 H), 7.86 (t, J = 8.84, 6.76 Hz, 1 H), 7.81 (d, J = 5.72 Hz, 1 H), 7.66 (m, 7 H), 7.40 (t, J = 7.12, 7.04 Hz, 2 H), 7.23 (t, J = 7.08, 7.12 Hz, 1 H). Anal. Calcd for $2(H_2O)$ $C_{39}H_{27}ClF_6N_5PRu$: C, 53.04; H, 3.54; N, 7.93 %. Found: C, 53.09; H, 3.57; N, 7.94 %. IR (Solid, cm^{-1}): $\nu(PF_6^-)$, 828, 548.

Synthesis of $[Ru^{II}(antpy)(bpy)(CH_3CN)](PF_6)_2$ [2]$(PF_6)_2$

The chloro complex [**1**](PF_6) (100 mg, 0.118 mmol) was placed in 15 mL of 1:1 water and acetonitrile mixture under argon saturated atmosphere and refluxed for 12 h. After reaction the initial purple colour was changed to deep orange. Then the solution was cooled and evaporated to a minimal volume. Addition of few drops of aqueous saturated KPF_6 resulted a brown colour

View Article Online
DOI: 10.1039/D0DT01788D

precipitate. After filtering the solid ppt, it was washed thrice (5 mL x 3) with cold water and dried in desiccator. Crude [**2**]$(PF_6)_2$ was purified by column chromatography using a neutral alumina column with 10 % CH_3CN/CH_2Cl_2 as eluent. Yield: 80.6 mg (68.46 %). MS (ESI^+, CH_3CN), *m/z* Calcd for $[M–PF_6]^+$: 853.122; Found 853.128. Molar conductivity [$\Lambda_M(\Omega^{-1}\,cm^2\,M^{-1})$] in CH_3CN at 298 K: 229. ^1H NMR (400 MHz, $(CD_3)_2SO$, Me_4Si): δ_H (ppm): 9.74 (d, J = 5.24 Hz, 1 H), 9.18 (s, 2 H), 9.02 (d, J = 8.24 Hz, 1 H), 8.95 (s, 1 H), 8.83 (d, J = 8.04 Hz, 2 H), 8.78 (d, J = 8.2 Hz, 1 H), 8.48 (t, J = 7.88, 7.8 Hz, 1 H), 8.33 (m, 2 H), 8.22 (d, J = 8.2, Hz, 1 H), 8.06 (m, 4 H), 7.80 (m, 4 H), 7.69 (m, 3 H), 7.59 (t, J = 8.56, 7.88 Hz, 1 H), 7.50 (t, J = 7.32, 7.08 Hz, 2 H), 7.38 (t, J = 7.16, 7.24 Hz, 1 H), 2.44 (s, 3 H). Anal. Calcd for (CH_3CN) $C_{41}H_{30}F_{12}N_6P_2Ru$: C, 49.72; H, 3.20; N, 9.44 %. Found: C, 49.7; H, 3.22; N, 9.47 %. IR (Solid, cm^{-1}): $\nu(PF_6^-)$, 830, 552.

Synthesis of $[Ru^{II}(antpy)(bpy)(NO_2)]PF_6$ [3](PF_6)

Excess sodium nitrite (190 mg, 2.75 mmol) was added after dissolving [**2**]$(PF_6)_2$ (100 mg, 0.1 mmol) in 15 mL hot acetone/water mixture and refluxed for 12 h. After the reaction the orange-coloured solution was changed to yellowish-red. Crystalline nitro complex was separated from solution after cooling to room temperature. Obtained solid as pure [**3**](PF_6) was filtered off and wash with cold water and dried in desiccator. Yield: 70 mg (81.6 %). MS (ESI^+, CH_3CN), *m/z* Calcd for $[M–PF_6]^+$: 713.124; Found 713.133. Molar conductivity [$\Lambda_M(\Omega^{-1}\,cm^2\,M^{-1})$] in CH_3CN at 298 K: 131. ^1H NMR (400 MHz, $(CD_3)_2SO$, Me_4Si): δ_H (ppm): 9.83 (d, J = 4.92 Hz, 1 H), 9.07 (s, 2 H), 8.97 (d, J = 8.2 Hz, 1 H), 8.94 (s, 1 H), 8.76 (m, 3 H), 8.41 (t, J = 7.88, 7.76 Hz, 1 H), 8.32 (t, J = 6.8, 7.48 Hz, 2 H), 8.23 (d, J = 8.32, 1 H), 8.10 (t, J = 7.12, 6.04, Hz, 1 H), 8.00 (m, 3 H), 7.90 (d, J = 5.16, 1 H), 7.76 (d, J = 4.92, 2 H), 7.66 (m, 5 H), 7.44 (t, J = 7.08, 6.08 Hz, 2 H), 7.36 (t, J = 6.04, 6.08 Hz, 1 H). Anal. Calcd for ($5H_2O$) $C_{39}H_{27}F_6N_6O_2PRu$: C, 49.42; H, 3.94; N, 8.87 %. Found: C, 49.41; H, 3.97; N, 8.81 %. IR (Solid, cm^{-1}): $\nu(PF_6^-)$, 833, 549; $\nu(Ru^{II}–NO_2)$, 1354, 1268.

Synthesis of $[Ru^{II}(antpy)(bpy)(NO^+)](PF_6)_3$ [4]$(PF_6)_3$

Conc. HNO_3 (2 mL) was dropwise added on solid [**3**](PF_6) (100 mg, 0.116 mmol) at 0 °C under the constant stirring condition to form a pasty mass. Conc. $HClO_4$ (4 mL) was added to the pasty mass carefully at 0 °C with stirring. After 2 min, a few drops of saturated aqueous KPF_6 solution were added, leading to the formation of yellow precipitate which was filtered off and washed carefully with about 10 mL of cold water and dried under argon atmosphere. Yield: 65.3 mg (49.74%). MS (ESI^+, CH_3CN), *m/z* Calcd for $[M–2PF_6]^+$: 842.09; Found 842.08. Molar

View Article Online
DOI: 10.1039/D0DT01788D

conductivity [$\Lambda_M(\Omega^{-1}\,cm^2\,M^{-1})$] in CH_3CN at 298 K: 343. ^1H NMR (400 MHz, $(CD_3)_2SO$, Me_4Si): δ_H (ppm): 9.84 (d, J = 5.2 Hz, 1 H), 9.15 (s, 2 H), 8.97 (d, J = 8.2 Hz, 1 H), 8.77 (t, J = 8.04, 7.8 Hz, 2 H), 8.71–8.68 (m, 2 H), 8.60 (d, J = 7.96 Hz, 2 H), 8.48–8.40 (m, 2 H), 8.34–8.31 (m, 1 H), 8.14–8.09 (m, 2 H), 8.04 (t, J = 8.96, 7.96 Hz, 3 H), 7.99–7.91 (m, 4 H), 7.78 (d, J = 4.68, 2 H), 7.47 (t, J = 7.12, 6.08 Hz, 2 H), 7.36–7.31 (m, 1 H). Anal. Calcd for ($10H_2O$) $C_{39}H_{27}F_6N_6O_2PRu$: C, 49.42; H, 3.94; N, 8.87. Found: C, 49.41; H, 3.97; N, 8.81 %. IR (Solid, cm^{-1}): $\nu(PF_6^-)$, 835, 554; $\nu(Ru^{II}–NO^+)$, 1941.

Synthesis of $[Ru^{II}(antpy)(bpy)(NO^{\bullet})](PF_6)_2$ [4]$(PF_6)_2$

In 2 mL acetone [**4**]$(PF_6)_3$ (50 mg, 0.04 mmol) was dissolved and excess hydrazine hydrate was added with stirring for 10 min under argon atmosphere. The yellow colour solution changed to deep red. Then the solvent was removed and the dark colour precipitate was obtained. The precipitate was washed with cold water and dried under argon. Yield: 20 mg (50.67 %). IR (Solid, cm^{-1}): $\nu(PF_6^-)$, 835, 552; $\nu(Ru^{II}–NO^{\bullet})$, 1612.

Photo-liberated NO trapping by Myoglobin

3 mL CH_3CN solution of [**4**]$(PF_6)_3$ was placed in a quartz cuvette and the cuvette was made air-tight after degassed thoroughly with an argon atmosphere. The photo-cleavage experiment was performed for ~ 2 h on exposure with visible 200 W Xenon light. The photo liberated NO gas was passed by using cannula through a solution containing aqueous reduced myoglobin and the electronic absorption spectra were measured. The same experiment was repeated with reduced species [**4**]$(PF_6)_2$ for ~70 min timescale. In the case of [**4**]$(PF_6)_3$ the photolysis experiment again performed with IR light source (>700 nm) at room temperature.

Crystallography

Single crystals of the nitro complex [**3**](PF_6) were grown at room temperature by slow evaporation of 1:2 toluene and acetone solvent mixtures. X-ray data were collected on Agilent Supernova dual-source diffractometer. The experiment was performed on Rigaku Supernova Xcalibur EOS CCD detector with graphite monochromatic Mo-Kα radiation (λ_α = 0.71073 Å). A suitable single crystal was mounted in a thin layer of inert mineral oil at 290 K. The structure was solved using direct methods SHELXT[69] and refined by full-matrix least-squares techniques on *F2* by using SHELXL using OLEX2.[70]Absorption corrections were carried out by following multi-scan technique. The identification of all non-hydrogen atoms has been achieved by multiple refinements along with

View Article Online
DOI: 10.1039/D0DT01788D

thermal parameters associated with anisotropy. The hydrogen atoms were located at idealized places allowed to ride on the nearest to the non-hydrogen atom.

Culture of VCaP prostate cancer cell line

The prostate cancer cell line VCaP was cultured in DMEM high glucose medium (Lonza) + 10 % fetal bovine serum (FBS) + 1% penicillin/streptomycin. Depending upon the assay, different number of cells were seeded in 6 and 96-well plates and were cultured at 37 ^{o}C in a 5 % CO_2 incubator until appropriate confluency to carry out the experiment was achieved.

Live Cell Imaging Experiments

Live-cell imaging experiments were carried out to understand the cytotoxic behaviour of the ruthenium nitrosyl complexes. 10^4 VCaP prostate cancer cells were grown in a 6-well plate in DMEM high glucose medium + 10 % FBS + 1% penicillin/streptomycin, for 24 h in the CO_2 incubator for the cells to attain 70-75 % confluency. Thereafter, the complexes [**1**](PF_6), [**2**]$(PF_6)_2$, [**3**](PF_6), [**4**]$(PF_6)_3$, and [**4**]$(PF_6)_2$ dissolved in DMSO were added to the cells at a final concentration of either 1 μM and 3 μM in dark, following which the cells were further incubated for 6 h at 37 ^{o}C in 5% CO_2 incubator. After the incubation period, the culture medium containing the compound was removed and the cells were washed multiple times with PBS to remove the residual compound. The cells were then photo-exposed for either 5, 10 and 15 min using a Xenon (200 W) bulb (400-700 nm) in PBS. After the photo-exposure, PBS was removed and fresh DMEM high glucose media was added to the cells and the bright field images were captured using the Nikon Inverted Research Microscope (ECLIPSE TS2R-FL) with the exposure time of 100 ms.

Photo-cytotoxicity Experiments

Photo-cytotoxicity of the ruthenium nitrosyl complex [**4**]$(PF_6)_3$ was determined using the colorimetric MTT assay. 1X 10^3 VCaP cells were seeded in 96-well plate containing DMEM high glucose medium + 10 % FBS + 1% penicillin/streptomycin. Cells were incubated at 37 ^{o}C for 12 h following which various concentrations of [**4**]$(PF_6)_3$ dissolved in 1% DMSO was added to the cells. The cells were incubated with [**4**]$(PF_6)_3$ for 6 h in dark, following which the medium was replaced with fresh PBS, and the cells were irradiated with visible light for 15 min using a Xenon 200 W light source. After the photo-exposure, PBS was removed and replaced with fresh DMEM high glucose medium + 10 % FBS + 1% penicillin/streptomycin, and the incubation was further continued for 1 h. Subsequently, 20 μL of 5 mg mL^{-1}MTT was added to each well and the plate

View Article Online
DOI: 10.1039/D0DT01788D

was incubated at 37 °C in the 5% CO_2 incubator for 3.5-4 h. For dissolving the formed formazan crystals, the culture medium was replaced with 200 µL of MTT solvent (4 mM HCl, 0.1% Nondet P-40 (NP-40) all in isopropanol) and absorbance was recorded at 595 nm using an iMark microplate absorbance reader. The cytotoxicity of [**4**]$(PF_6)_3$ was measured as a ratio of the absorbance of treated cells to the untreated control at 595 nm. The IC_{50} value was determined by non-linear regression analysis using Graphpad prism.

Conflicts of interest

There are no conflicts to declare.

Acknowledgment

(SERB, project no. ECR/2016/000382) (fellowship to S.K.), Council of Scientific and Industrial Research (CSIR) (fellowship to B.G., K.S., and A.M.) and IIT Hyderabad are gratefully acknowledged for the financial support. Taruna Saini acknowledges fellowship support from MHRD. Ashish Misra acknowledges financial support from SERB (project no. ECR/2017/002544) and IIT Hyderabad. We sincerely thank to Ms. Suparna Basu for helpful discussion.

View Article Online
DOI: 10.1039/D0DT01788D

References

1 J. S. Stamler, D. J. Singel and J. Loscalzo, *Science*, 1992, **258**, 1898–1902.

2 J. A. McCleverty, *Chem. Rev.*, 2004, **104**, 403–418.

3 H. P. Monteiro, E. G. Rodrigues, A. K. C. Amorim Reis, L. S. Longo, F. T. Ogata, A. I. S. Moretti, P. E. da Costa, A. C. S. Teodoro, M. S. Toledo and A. Stern, *Nitric Oxide*, 2019, **89**, 1–13.

4 Z. J. Tonzetich, L. E. McQuade and S. J. Lippard, *Inorg. Chem.*, 2010, **49**, 6338–6348.

5 A. P. Castano, P. Mroz and M. R. Hamblin, *Nature Reviews Cancer*, 2006, **6**, 535.

6 G. B. Richter-Addo, P. Legzdins and J. Burstyn, *Chem. Rev.*, 2002, **102**, 857–860.

7 J. C. B. Ferreira and D. Mochly-Rosen, *Circulation Journal*, 2012, **76**, 15–21.

8 N. L. Fry and P. K. Mascharak, *Acc. Chem. Res.*, 2011, **44**, 289–298.

9 M. H. Al-Afyouni, T. N. Rohrabaugh, K. F. Al-Afyouni and C. Turro, *Chem. Sci.*, 2018, **9**, 6711–6720.

10 J. D. Knoll and C. Turro, *Coordination Chemistry Reviews*, 2015, **282–283**, 110–126.

11 P. Singh, B. Sarkar, M. Sieger, M. Niemeyer, J. Fiedler, S. Záliš and W. Kaim, *Inorg. Chem.*, 2006, **45**, 4602–4609.

12 K. Ghosh, R. Kumar, S. Kumar and J. S. Meena, *Dalton Trans.*, 2013, **42**, 13444–13452.

13 F. Roncaroli, M. Videla, L. D. Slep and J. A. Olabe, *Coordination Chemistry Reviews*, 2007, **251**, 1903–1930.

14 M. Wolak, A. Zahl, T. Schneppensieper, G. Stochel and R. van Eldik, *J. Am. Chem. Soc.*, 2001, **123**, 9780–9791.

15 L. E. Laverman, A. Wanat, J. Oszajca, G. Stochel, P. C. Ford and R. van Eldik, *J. Am. Chem. Soc.*, 2001, **123**, 285–293.

16 A. K. Patra, J. M. Rowland, D. S. Marlin, E. Bill, M. M. Olmstead and P. K. Mascharak, *Inorg. Chem.*, 2003, **42**, 6812–6823.

17 R. K. Afshar, A. K. Patra, M. M. Olmstead and P. K. Mascharak, *Inorg. Chem.*, 2004, **43**, 5736–5743.

18 F. P. Rodrigues, Z. A. Carneiro, P. Mascharak, C. Curti and R. S. da Silva, *Coordination Chemistry Reviews*, 2016, **306**, 701–707.

19 T. C. Berto, A. L. Speelman, S. Zheng and N. Lehnert, *Coordination Chemistry Reviews*, 2013, **257**, 244–259.

View Article Online
DOI: 10.1039/D0DT01788D

20 A. B. McQuarters, J. W. Kampf, E. E. Alp, M. Hu, J. Zhao and N. Lehnert, *Inorg. Chem.*, 2017, **56**, 10513–10528.

21 A. K. Patra, J. M. Rowland, D. S. Marlin, E. Bill, M. M. Olmstead and P. K. Mascharak, *Inorg. Chem.*, 2003, **42**, 6812–6823.

22 P. Labra-Vázquez, M. Bocé, M. Tassé, S. Mallet-Ladeira, P. G. Lacroix, N. Farfán and I. Malfant, *Dalton Trans.*, 2020, **49**, 3138–3154.

23 E. Tfouni, D. R. Truzzi, A. Tavares, A. J. Gomes, L. E. Figueiredo and D. W. Franco, *Nitric Oxide*, 2012, **26**, 38–53.

24 E. Orlowska, M. V. Babak, O. Dömötör, E. A. Enyedy, P. Rapta, M. Zalibera, L. Bučinský, M. Malček, C. Govind, V. Karunakaran, Y. C. S. Farid, T. E. McDonnell, D. Luneau, D. Schaniel, W. H. Ang and V. B. Arion, *Inorg. Chem.*, 2018, **57**, 10702–10717.

25 T. M. Bastos, M. I. F. Barbosa, M. M. da Silva, J. W. da C. Júnior, C. S. Meira, E. T. Guimaraes, J. Ellena, D. R. M. Moreira, A. A. Batista and M. B. P. Soares, *Antimicrob Agents Chemother*, 2014, **58**, 6044–6055.

26 R. Kumar, A. Yadav, A. Ratnam, S. Kumar, M. Bala, D. Sur, S. Narang, U. P. Singh, P. K. Mandal and K. Ghosh, *European Journal of Inorganic Chemistry*, 2017, **2017**, 5334–5343.

27 E. C. Constable and D. R. Smith, *Supramolecular Chemistry*, 1994, **4**, 5–7.

28 G. Albano, V. Balzani, E. C. Constable, M. Maestri and D. R. Smith, *Inorganica Chimica Acta*, 1998, **277**, 225–231.

29 M. N. Patel, D. S. Gandhi, P. A. Parmar and H. N. Joshi, *Journal of Coordination Chemistry*, 2012, **65**, 1926–1936.

30 H.-Y. Ding, X.-S. Wang, L.-Q. Song, J.-R. Chen, J.-H. Yu, Chao-Li and B.-W. Zhang, *Journal of Photochemistry and Photobiology A: Chemistry*, 2006, **177**, 286–294.

31 J. Wang, E. A. Medlycott, G. S. Hanan, F. Loiseau and S. Campagna, *Inorganica Chimica Acta*, 2007, **360**, 876–884.

32 D. Maity, S. Das, S. Mardanya and S. Baitalik, *Inorg. Chem.*, 2013, **52**, 6820–6838.

33 J. Wang, G. S. Hanan, F. Loiseau and S. Campagna, *Chem. Commun.*, 2004, **0**, 2068–2069.

34 V. Singh, K. Sharma, B. Shankar, S. K. Awasthi and R. D. Gupta, *New J. Chem.*, 2016, **40**, 5906–5913.

35 D. Maheshwaran, T. Nagendraraj, P. Manimaran, B. Ashokkumar, M. Kumar and R. Mayilmurugan, *European Journal of Inorganic Chemistry*, 2017, **2017**, 1007–1016.

View Article Online
DOI: 10.1039/D0DT01788D

36 S. Roy, S. Roy, S. Saha, R. Majumdar, R. R. Dighe, E. D. Jemmis and A. R. Chakravarty, *Dalton Trans.*, 2011, **40**, 1233–1242.

37 U. Basu, I. Khan, D. Koley, S. Saha, P. Kondaiah and A. R. Chakravarty, *Journal of Inorganic Biochemistry*, 2012, **116**, 77–87.

38 S.-Y. Jiao, K. Li, W. Zhang, Y.-H. Liu, Z. Huang and X.-Q. Yu, *Dalton Trans.*, 2014, **44**, 1358–1365.

39 Z. Dai, L. Tian, Y. Xiao, Z. Ye, R. Zhang and J. Yuan, *J. Mater. Chem. B*, 2013, **1**, 924–927.

40 Y. Liu, H. Dong, W. Zhang, Z. Ye, G. Wang and J. Yuan, *Biosensors and Bioelectronics*, 2010, **25**, 2375–2378.

41 J. Wu, Y. Xing, H. Wang, H. Liu, M. Yang and J. Yuan, *New J. Chem.*, 2017, **41**, 15187–15194.

42 A. Kumar, *Journal of Inorganic Biochemistry*, 2017, **176**, 134–139.

43 A. Genoni, D. N. Chirdon, M. Boniolo, A. Sartorel, S. Bernhard and M. Bonchio, *ACS Catal.*, 2017, **7**, 154–160.

44 F. Guo and W. Sun, *J. Phys. Chem. B*, 2006, **110**, 15029–15036.

45 A. Kumar, I. Pant, A. Dixit, S. Banerjee, B. Banik, R. Saha, P. Kondaiah and A. R. Chakravarty, *Journal of Inorganic Biochemistry*, 2017, **174**, 45–54.

46 K. Choroba, B. Machura, L. R. Raposo, J. G. Małecki, S. Kula, M. Pająk, K. Erfurt, A. M. Maroń and A. R. Fernandes, *Dalton Trans.*, 2019, **48**, 13081–13093.

47 U. Basu, I. Khan, A. Hussain, P. Kondaiah and A. R. Chakravarty, *Angewandte Chemie International Edition*, 2012, **51**, 2658–2661.

48 A. Szlapa-Kula, M. Małecka and B. Machura, *Dyes and Pigments*, 2020, **180**, 108480.

49 S. Sen, B. Kawahara, N. L. Fry, R. Farias-Eisner, D. Zhang, P. K. Mascharak and G. Chaudhuri, *Archives of Biochemistry and Biophysics*, 2013, **540**, 33–40.

50 B. P. Sullivan, J. M. Calvert and T. J. Meyer, *Inorg. Chem.*, 1980, **19**, 1404–1407.

51 J. Pitarch López, F. W. Heinemann, R. Prakash, B. A. Hess, O. Horner, C. Jeandey, J.-L. Oddou, J.-M. Latour and A. Grohmann, *Chemistry – A European Journal*, 2002, **8**, 5709–5722.

52 S. Maji, B. Sarkar, M. Patra, A. K. Das, S. M. Mobin, W. Kaim and G. K. Lahiri, *Inorg. Chem.*, 2008, **47**, 3218–3227.

View Article Online
DOI: 10.1039/D0DT01788D

53 N. Chanda, S. M. Mobin, V. G. Puranik, A. Datta, M. Niemeyer and G. K. Lahiri, *Inorg. Chem.*, 2004, **43**, 1056–1064.

54 S. Sarkar, B. Sarkar, N. Chanda, S. Kar, S. M. Mobin, J. Fiedler, W. Kaim and G. K. Lahiri, *Inorg. Chem.*, 2005, **44**, 6092–6099.

55 P. De, T. K. Mondal, S. M. Mobin, B. Sarkar and G. K. Lahiri, *Inorganica Chimica Acta*, 2010, **363**, 2945–2954.

56 E. Sondaz, A. Gourdon, J.-P. Launay and J. Bonvoisin, *Inorganica Chimica Acta*, 2001, **316**, 79–88.

57 P. De, S. Maji, A. D. Chowdhury, S. M. Mobin, T. K. Mondal, A. Paretzki and G. K. Lahiri, *Dalton Trans.*, 2011, **40**, 12527–12539.

58 B. Giri, S. Kumbhakar, K. Kalai Selvan, A. Muley and S. Maji, *Inorganica Chimica Acta*, 2020, **502**, 119360.

59 N. L. Fry, B. J. Heilman and P. K. Mascharak, *Inorg. Chem.*, 2011, **50**, 317–324.

60 M. Roose, M. Tassé, P. G. Lacroix and I. Malfant, *New J. Chem.*, 2019, **43**, 755–767.

61 S. Maji, C. Chatterjee, S. M. Mobin and G. K. Lahiri, *European Journal of Inorganic Chemistry*, 2007, **2007**, 3425–3434.

62 G. M. Halpenny, M. M. Olmstead and P. K. Mascharak, *Inorg. Chem.*, 2007, **46**, 6601–6606.

63 A. C. Merkle, A. B. McQuarters and N. Lehnert, *Dalton Trans.*, 2012, **41**, 8047–8059.

64 S. V. Jovanovic and M. G. Simic, *J. Phys. Chem.*, 1986, **90**, 974–978.

65 S. Steenken and S. V. Jovanovic, *J. Am. Chem. Soc.*, 1997, **119**, 617–618.

66 S. V. Jovanovic and M. G. Simic, *Biochimica et Biophysica Acta (BBA) - Gene Structure and Expression*, 1989, **1008**, 39–44.

67 H. Xie, D. Yang, A. Heller and Z. Gao, *Biophysical Journal*, 2007, **92**, L70–L72.

68 D. Kondrikov, F. V. Fonseca, S. Elms, D. Fulton, S. M. Black, E. R. Block and Y. Su, *J. Biol. Chem.*, 2010, **285**, 4319–4327.

69 G. M. Sheldrick, *Acta Cryst A*, 2015, **71**, 3–8.

70 G. M. Sheldrick, *Acta Cryst C*, 2015, **71**, 3–8.

71 P. De, T. K. Mondal, S. M. Mobin and G. K. Lahiri, *Inorganica Chimica Acta*, 2011, **372**, 250–258.

View Article Online
DOI: 10.1039/D0DT01788D

72 M. Videla, J. S. Jacinto, R. Baggio, M. T. Garland, P. Singh, W. Kaim, L. D. Slep and J. A. Olabe, *Inorg Chem*, 2006, **45**, 8608–8617.

73 P. Singh, J. Fiedler, S. Záliš, C. Duboc, M. Niemeyer, F. Lissner, T. Schleid and W. Kaim, *Inorg. Chem.*, 2007, **46**, 9254–9261.

74 D. W. Pipes and T. J. Meyer, *Inorg. Chem.*, 1984, **23**, 2466–2472.

75 B. Mondal, H. Paul, V. G. Puranik and G. K. Lahiri, *J. Chem. Soc., Dalton Trans.*, 2001, **0**, 481–487.

76 A. Dovletoglou, S. A. Adeyemi and T. J. Meyer, *Inorg. Chem.*, 1996, **35**, 4120–4127.

View Article Online
DOI: 10.1039/D0DT01788D

Table 1. Crystallographic parameters of [3](PF$_6$)

Complex	[**3**](PF$_6$)
Empirical formula	$C_{39}H_{27}N_6O_2F_6PRu$
Formula weight	857.70
Crystal system	Monoclinic
Space group	$P2_1/c$
a (Å)	15.9066(4)
b (Å)	22.4041(6)
c (Å)	14.3001(3)
α (deg)	90
β (deg)	90.642(2)
γ (deg)	90
V (Å^3)	5095.9(2)
Z	5
T (K)	290
μ (mm^{-1})	0.491
ρ_{calcd} (g cm^{-3})	1.397
F (000)	2160.0
2θ range (deg)	4.448 to 57.968
data/restraints/parameters	10532/0/496
R_1, wR_2 [$I > 2\sigma(I)$]	$R_1 = 0.0636$, $wR_2 = 0.1720$
R_1, wR_2 (all data)	$R_1 = 0.0975$, $wR_2 = 0.1953$
Goodness-of-fit on F^2	0.984
Largest difference between peak and hole (e Å^{-3})	0.53/-0.44

View Article Online
DOI: 10.1039/D0DT01788D

Table 2. Selected bond distances (Å) and bond angles (°) for [3](PF$_6$)

Bond distance / Bond angle	[**3**](PF$_6$)
Ru1–N1	2.068(4)
Ru1–N2	1.969(3)
Ru1–N3	2.086(4)
Ru1–N4	2.081(5)
Ru1–N5	2.077(4)
Ru1–N6	2.027(4)
O1–N6	1.262(7)
O2–N6	1.215(6)
O1–N6–O2	119.1(5)
N1–Ru1–N2	79.9(1)
N2–Ru1–N3	78.4(1)
N1–Ru1–N3	158.3(1)
N4–Ru1–N5	77.7(2)
N1–Ru1–N6	90.0(2)
N2–Ru1–N6	88.0(2)
N3–Ru1–N6	89.0(2)
N4–Ru1–N6	95.7(2)
N5–Ru1–N6	173.0(2)
N5–Ru1–N1	93.2(1)
N5–Ru1–N2	98.7(1)
N5–Ru1–N3	90.3(1)
N2–Ru1–N4	175.4(1)
N3–Ru1–N4	104.4(2)
N1–Ru1–N4	97.3(2)

View Article Online
DOI: 10.1039/D0DT01788D

Table 3. Electronic Spectral Data of the complexes, recorded in acetonitrile solvent

Complex	λ(nm) [ε ($M^{-1}cm^{-1}$)]
[**1**](PF_6)	508[13486], 384[14806], 365[16363], 318[34065], 292[39138], 284[45941]
[**2**](PF_6)$_2$	460[15817], 384[11618], 364[12216], 329[23115], 308[40087], 284[53731]
[**3**](PF_6)	478[14378], 384[11940], 365[13948], 312[38718], 284[47772], 275[45592]
[**4**](PF_6)$_3$	362[16540], 332[18316], 294[40612]
[**4**](PF_6)$_2$	485[13582], 428[13134], 312[41080], 284[70089], 274[77875]

Table 4. IR vibrational frequencies and redox potentials

Complexes	ν(NO) cm^{-1}	*E* / V (Ru^{II}–NO^+/ Ru^{II}–$NO^{\bullet}$)	*E* / V (Ru^{II}– $NO^{\bullet}$/ Ru^{II}–NO^-)	Ref.
[Ru(tpm)(**L^1**)(NO^+)]$^{3+}$	1962	0.60	–0.07	ref[71]
[Ru(tpm)(**L^3**)(NO^+)]$^{3+}$	1959	0.55	–0.24	ref[72]
[Ru(tpy)(**L^2**)(NO^+)]$^{3+}$	1957	0.55	–0.09	ref[73]
[Ru(tpy)(**L^3**)(NO^+)]$^{3+}$	1952	0.45	–0.20	ref[74]
[Ru(tpy)(**L^1**)(NO^+)]$^{3+}$	1960	0.72	0.07	ref[75]
[Ru(tpy)(**L^4**)(NO^+)]$^{3+}$	1948	0.49	–0.26	ref[52]
[Ru([9]aneS_3)(**L^3**)(NO^+)]$^{3+}$	1945	0.49	0.07	ref[57]
[Ru([9]aneS_3)(**L^1**)(NO^+)]$^{3+}$	1964	0.67	0.03	ref[57]
[Ru(tpy)(**L^5**)(NO^+)]$^{3+}$	1914	0.02 (in CH_2Cl_2)	–0.75 (in CH_2Cl_2)	ref[76]
[Ru(antpy)(**L^3**)(NO^+)]$^{3+}$	1941	0.46	–0.17	Present work

View Article Online
DOI: 10.1039/D0DT01788D

Table 5. Redox potential values of complexes[a,b]

Complex	Couple			antpy reduction	
	Ru^{III}/Ru^{II}	$NO^{+}\rightarrow NO^{\bullet}$	$NO^{\bullet}\rightarrow NO^{-}$		
[**1**](PF_6)	0.806(67)			–1.390(63)	–1.596(142)
[**2**]$(PF_6)_2$	1.327(155)			–1.234(75)	–1.402(177)
[**3**](PF_6)	1.052(75)			–1.344(51)	–1.670(137)
[**4**]$(PF_6)_3$		0.464(72)	–0.177(114)[b]	–0.621(118)	–1.178(198)

[a]Potentials $E°_{298K/V}$ in volt (ΔE[mV]) versus SCE in CH_3CN/0.1 M $^{n}Bu_4NClO_4$. [b]Quasi-reversible

View Article Online
DOI: 10.1039/D0DT01788D

Figure captions

Fig. 1. X-ray crystal structure of $[Ru^{II}(antpy)(bpy)(NO_2)](PF_6)$ [**3**](PF_6); Ellipsoids with 40% probability. Hydrogen atoms and counter anion are omitted for better clarity.

Fig. 2. Electronic spectra of complexes [**1**](PF_6), [**2**]$(PF_6)_2$, [**3**](PF_6), [**4**]$(PF_6)_3$ and [**4**]$(PF_6)_2$. The spectra were recorded in CH_3CN solvent at 298 K.

Fig. 3. FTIR (solid) spectra of [**4**]$(PF_6)_3$ (black) and [**4**]$(PF_6)_2$ (Red).

Fig. 4. CV of [**4**]$(PF_6)_3$, recorded in dry CH_3CN in presence of 0.1 M TBAP *vs* SCE with scan rate 50 mVs^{-1}(left). Least-squares plot, $E°$(V) of $[(Ru^{II}–NO^+)\rightarrow(Ru^{II}–NO^{\bullet})]$ *vs* ν(NO) / cm^{-1} of the related listed complexes in Table 4 (right).

Fig. 5. (a) The electronic spectrum of the photo-triggered NO release from complex [**4**]$(PF_6)_3$ (recorded in each 10 min intervals). (b) The electronic spectrum of the photo-triggered NO release from complex [**4**]$(PF_6)_2$ (recorded in each 3 min intervals). In the inset, the absorbance *vs* time plot corresponds at 460 nm (the solvate species) for both. (c) The electronic spectrum of the final spectrum after photolysis in CH_3CN from [**4**]$(PF_6)_3$ and isolated spectrum [**2**]$(PF_6)_2$ in CH_3CN.

Fig. 6. The electronic spectrum of IR light-triggered NO release from complex [**4**]$(PF_6)_3$ (recorded in each 5 min intervals). Inset is the absorbance *vs* time plot, monitored at 460 nm (the solvate species).

Fig. 7. Electronic spectra of reduced myoglobin (red), myoglobin (black), and NO adducted myoglobin (blue). The spectra were recorded in mili-Q water at room temperature.

Figure 8. Biological reduction of [**4**]$(PF_6)_3$ to [**4**]$(PF_6)_2$ by using an aqueous solution of Salmon sperm DNA (left) and oligonucleotide (used for expressing human β–actin) having sequence CAAGGCCAACCGCGAGAAGATGAC (right).

Fig. 9. Bright-field images of VCaP cells treated with [**4**]$(PF_6)_3$. (A) DMSO treated VCaP cells before photoirradiation. (B). DMSO treated VCaP cells following photoirradiation. (C) 1 μM [**4**]$(PF_6)_3$ treated VCaP cells before photoirradiation. (D) 1 μM [**4**]$(PF_6)_3$ treated VCaP cells following photoirradiation. (E) 3 μM ([**4**]$(PF_6)_3$ treated VCaP cells before photo-irradiation. (F) 3 μM [**4**]$(PF_6)_3$ treated VCaP cells following photo-irradiation.

Fig. 10. Effect of visible light exposure on VCaP prostate cancer cell line in the presence of [**4**]$(PF_6)_3$.

View Article Online
DOI: 10.1039/D0DT01788D

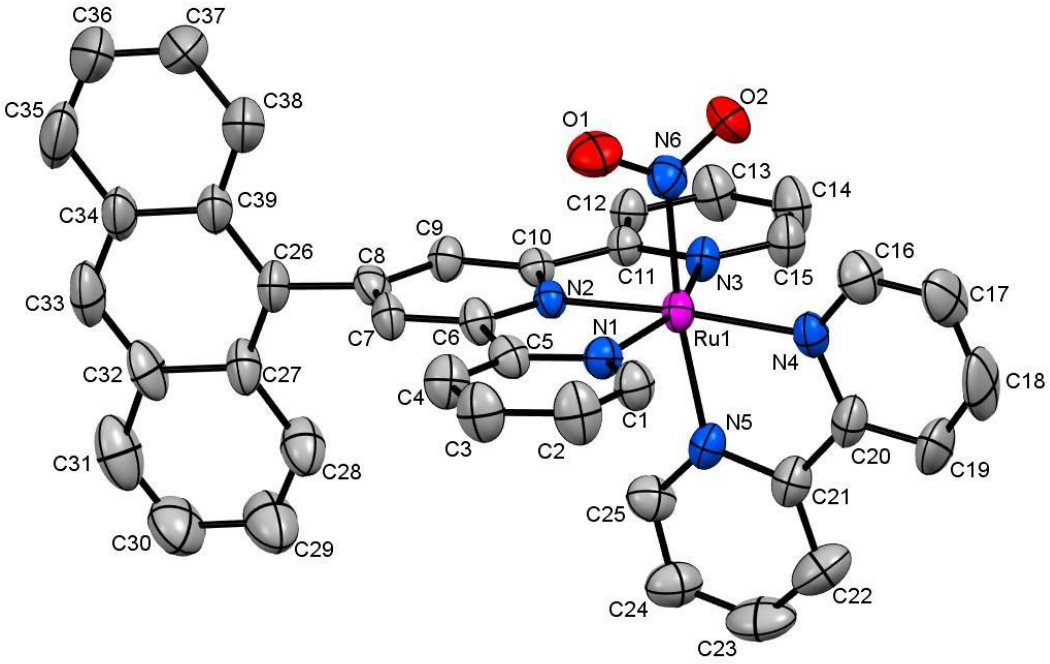

Fig. 1

View Article Online
DOI: 10.1039/D0DT01788D

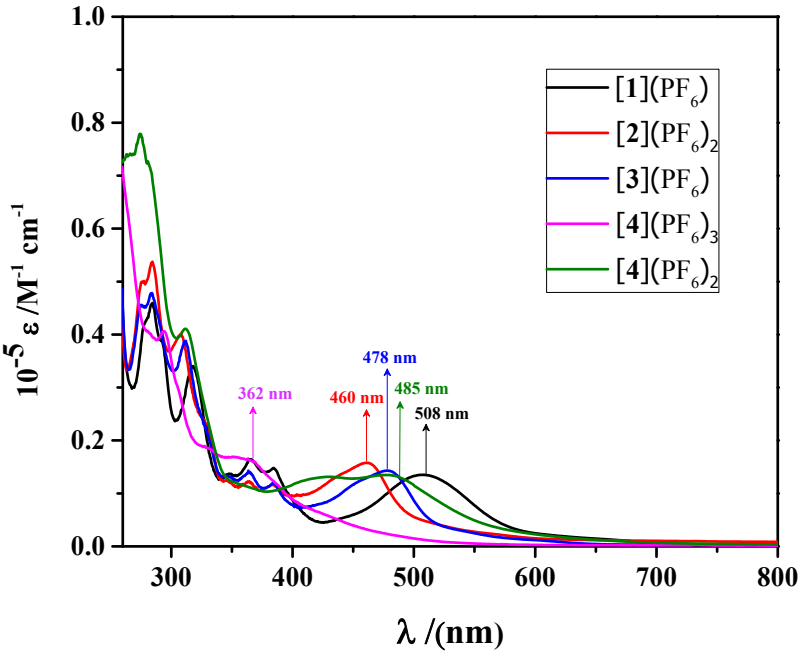

Fig. 2

View Article Online
DOI: 10.1039/D0DT01788D

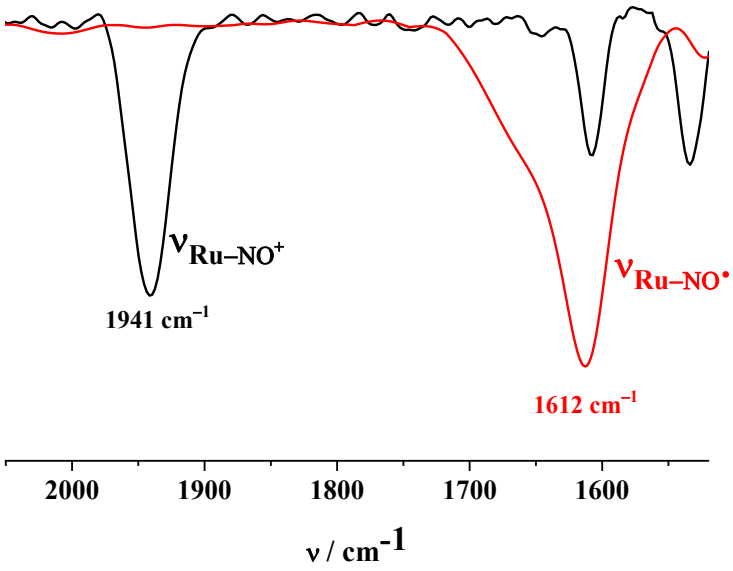

Fig. 3

View Article Online
DOI: 10.1039/D0DT01788D

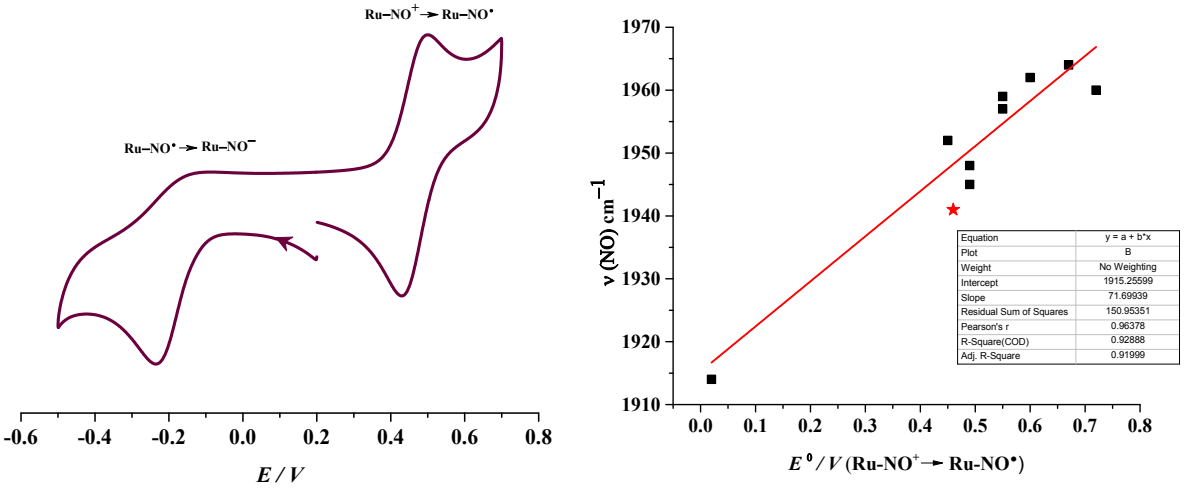

Fig. 4

View Article Online
DOI: 10.1039/D0DT01788D

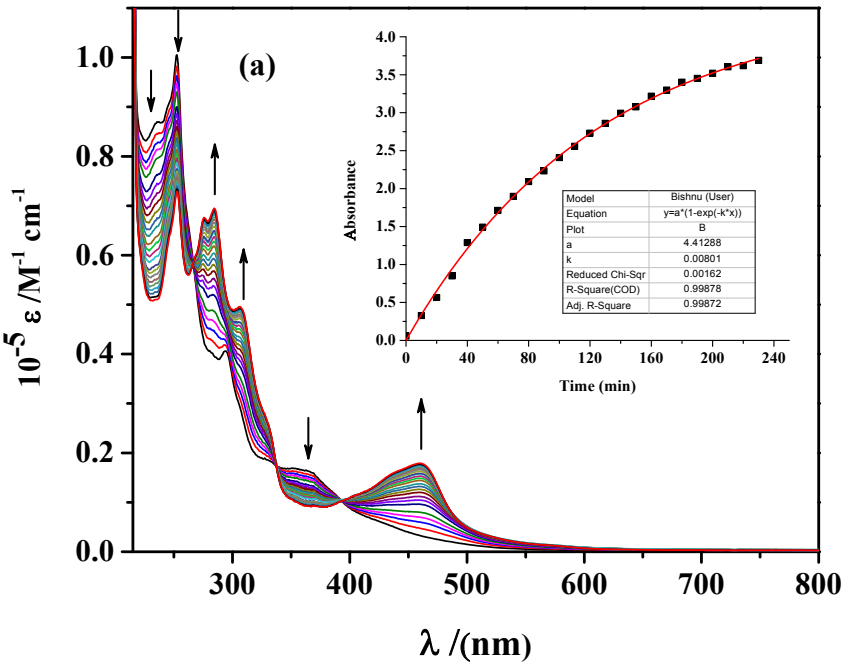

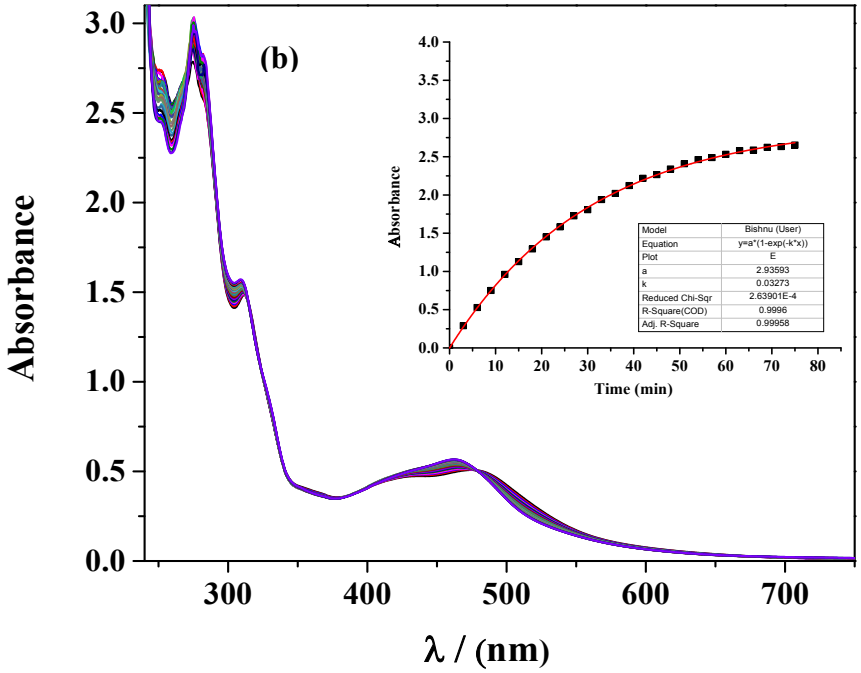

View Article Online
DOI: 10.1039/D0DT01788D

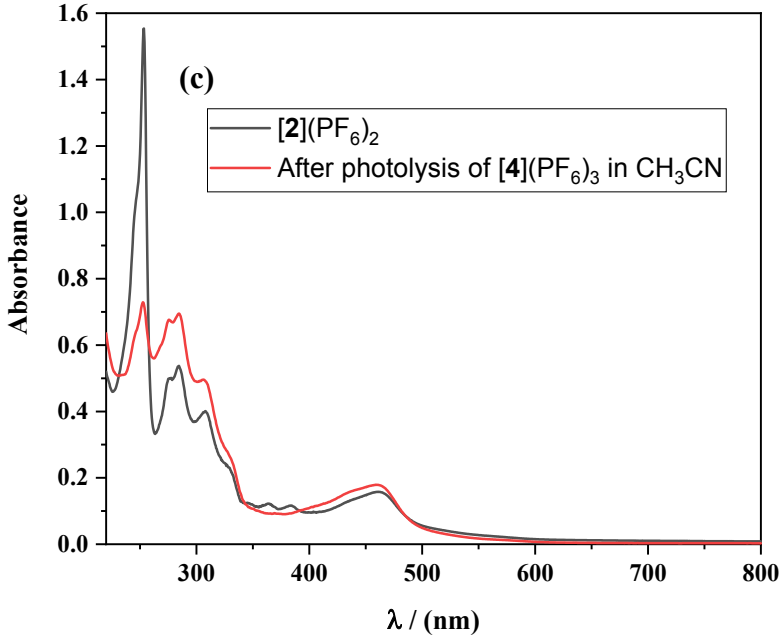

Fig. 5

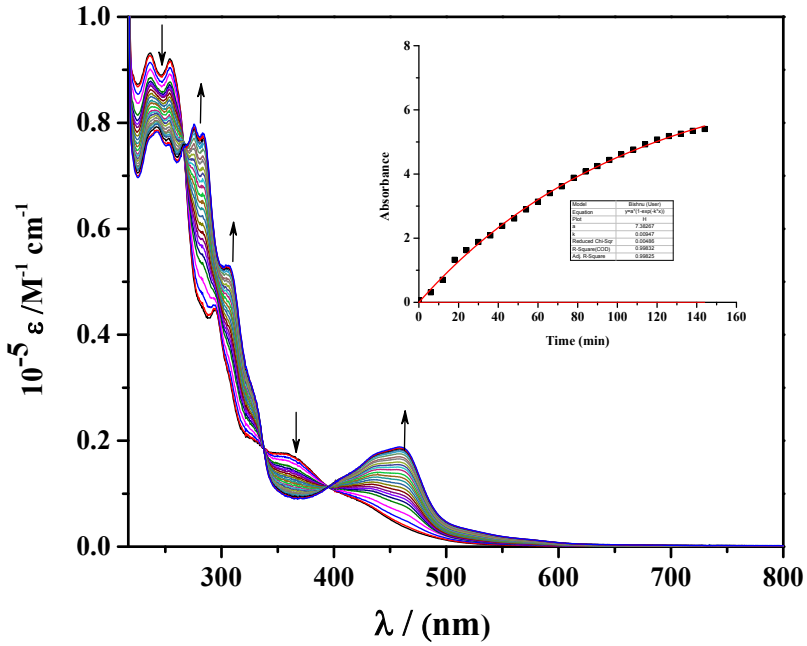

View Article Online
DOI: 10.1039/D0DT01788D

Fig. 6

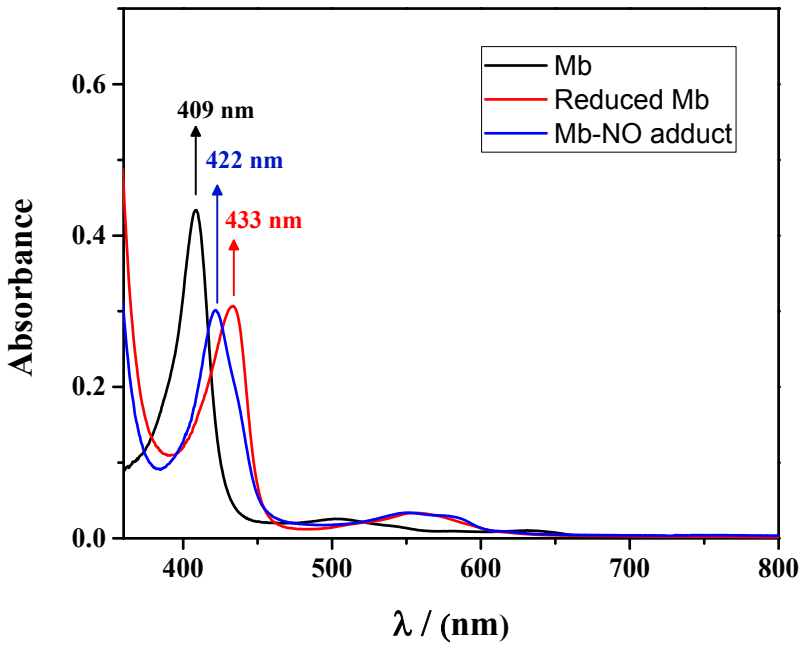

Fig. 7

View Article Online
DOI: 10.1039/D0DT01788D

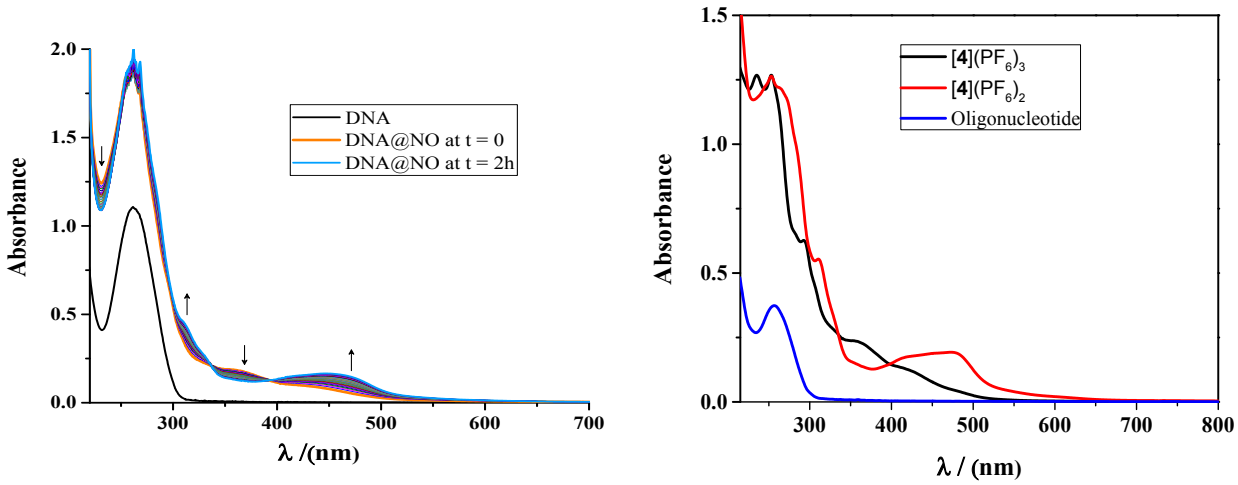

Fig. 8

View Article Online
DOI: 10.1039/D0DT01788D

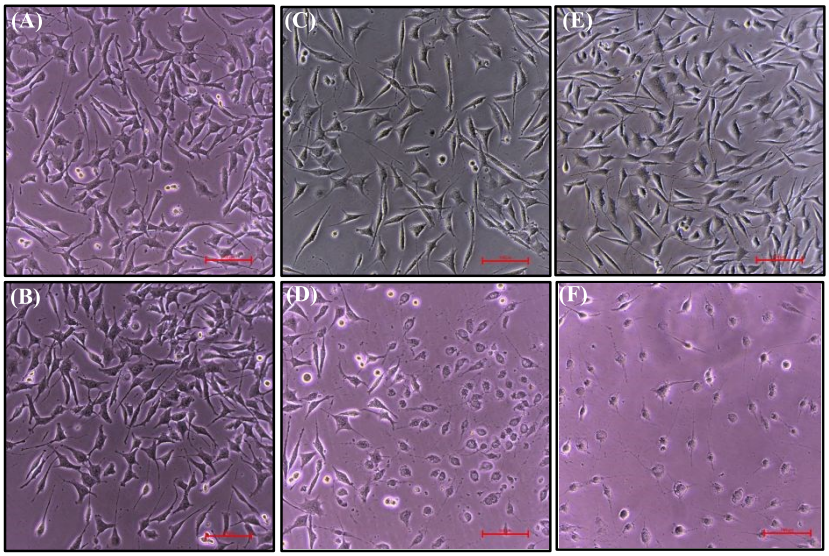

Fig. 9

View Article Online
DOI: 10.1039/D0DT01788D

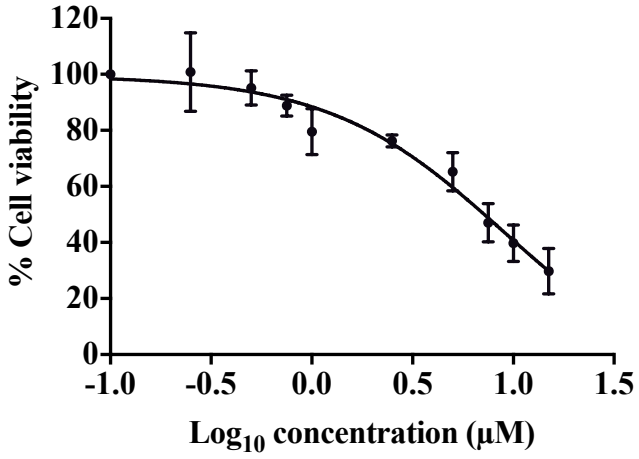

Fig. 10

View Article Online
DOI: 10.1039/D0DT01788D

Graphical abstract

Ruthenium nitrosyl complexes with molecular framework $[Ru^{II}(antpy)(bpy)NO^{+/\bullet}]^{n+}$ [**4**]$(PF_6)_3$ (n = 3), [**4**]$(PF_6)_2$ (n = 2) where antpy = 4'-(anthracen-9-yl)-2,2':6',2''-terpyridine and bpy = 2,2'-bipyridine) have been synthesized for efficient NO photorelease and [**4**]$(PF_6)_3$ exhibits significant phototoxicity upon irradiation with the visible light in the VCaP prostate cancer cell line.